Astronomy & Astrophysics manuscript no. my35paper
February 2, 2021

Seasonal reappearance of HCl in the atmosphere of Mars during the Mars year 35 dusty season

K. S. Olsen[1], A. Trokhimovskiy[2], L. Montabone[3,4], A. A. Fedorova[2], M. Luginin[2], F. Lefèvre[5], O. I. Korablev[2], F. Montmessin[5], F. Forget[4], E. Millour[4], A. Bierjon[4], L. Baggio[5], J. Alday[1], C. F. Wilson[1], P. G. J. Irwin[1], D. A. Belyaev[2], A. Patrakeev[2], and A. Shakun[2]

[1] Department of Physics, University of Oxford, Oxford, UK
e-mail: Kevin.Olsen@physics.ox.ac.uk
[2] Space Research Institute (IKI), Moscow, Russia
[3] Space Science Institute, Boulder, USA
[4] Laboratoire Atmosphères, Milieux, Observations Spatiales (LATMOS/CNRS), Paris, France
[5] Laboratoire de Météorologie Dynamique (LMD/CNRS), Paris, France

Received January 12, 2021

ABSTRACT

HCl was discovered in the atmosphere of Mars for the first time during the global dust storm in Mars year (MY) 34 (July 2018) using the Atmospheric Chemistry Suite mid-infrared channel (ACS MIR) on the ExoMars Trace Gas Orbiter. The simultaneity of variations in dust and HCl, and a correlation between water vapour and HCl, led to the proposal of a novel surface-atmosphere coupling analogous to terrestrial HCl production in the troposphere from salt aerosols. After seasonal dust activity restarted in MY 35 (August 2020), we have been monitoring HCl activity to determine whether such a coupling was validated. Here we present a new technique for analyzing the absorption features of trace gases close to the ACS MIR noise level and report that HCl mixing ratios are observed to rapidly increase in both hemispheres coincidentally with the onset of the MY 35 perihelion dust season. We present the temporal evolution of the vertical distribution of HCl (0.1–6 ppbv) and of dust activity in both hemispheres. We also report two observations of > 2 ppbv HCl below 10 km in the northern hemisphere during the aphelion period.

1. Introduction

The primary objective of the ExoMars Trace Gas Orbiter (TGO) is to detect any previously unknown trace gases diagnostic of active geological or biological processes. The recent discovery of HCl made using the Atmospheric Chemistry Suite mid-infrared channel (ACS MIR) was the first such finding for the TGO mission (Korablev et al. 2020). HCl had been a TGO target gas at Mars due to its relationship with active volcanism on Earth. Since seismic activity on Mars is low (Giardini et al. 2020) and no other gases related to volcanism (sulphur species or methane) have been identified concomitantly, the TGO observations are likely not indicative of active volcanism or subsurface magmatic outgassing, though such activity is not ruled out. The widespread distribution of HCl, and its time correlation with dust activity led us to suggest an alternate scenario in which there is a direct coupling between surface minerals and atmospheric trace gases. Such an interaction has implications for surface mineralogy since these observations imply that there is a frequent recycling between surface and atmospheric chlorine reservoirs.

The apparent simultaneity between the Mars year (MY) 34 global dust storm (GDS) and the first detection of HCl was a one-time correlation. No HCl was detected prior to the MY 34 GDS, nor after the dust season ended (upper limits < 0.1 ppbv) (Korablev et al. 2020). After L_s = 180° in MY 35, seasonal dust activity began again, and was followed after L_s = 203° by definitive HCl detections in ACS MIR observations. This supports the apparent, yet unproven, link between dust and HCl formation. Such a process would be analogous to terrestrial processes that convert solid-phase chloride minerals to gas-phase HCl in the troposphere (e.g., George & Abbatt 2010; Simpson et al. 2015).

The TGO entered Mars orbit in October 2016 and ACS MIR science observations began in April 2018 on solar longitude (L_s) 163° in MY 34. Within two months, around L_s = 190°, Mars was encircled in a global dust storm (e.g., Kass et al. 2019; Smith 2019). This was followed by a second, smaller storm around L_s = 320° and the dust opacity remained high enough to obscure low-altitude ACS MIR observations until after L_s = 350° (Montabone et al. 2020; Korablev et al. 2020). Dust was lofted to altitudes of 60–70 km (Luginin et al. 2020; Korablev et al. 2020) causing strong warming and expansion of the lower atmosphere (Fedorova et al. 2020; Aoki et al. 2019). HCl was first observed by ACS MIR with VMRs in the range of 1–4 ppbv below 35 km between L_s = 200–350° (Korablev et al. 2020).

Herein, we present new observations made during MY 35 by ACS MIR showing the return of 1–5 ppbv of HCl immediately following the increase in dust activity in the MY 35 perihelion dust season. This is similar to the quantities observed in MY 34 and we will show that the dust activity during most of the perihelion periods (after L_s = 240°) was similar in both Mars years. We have exploited the surface area of the ACS MIR detector array to reduce spectral noise and make more accurate measurements of HCl VMRs. This enabled two detections of HCl in the lower atmosphere during northern summer (aphelion).

2. Observations

The ACS MIR instrument is a cross-dispersion spectrometer operating in solar occultation geometry. It consists of a primary

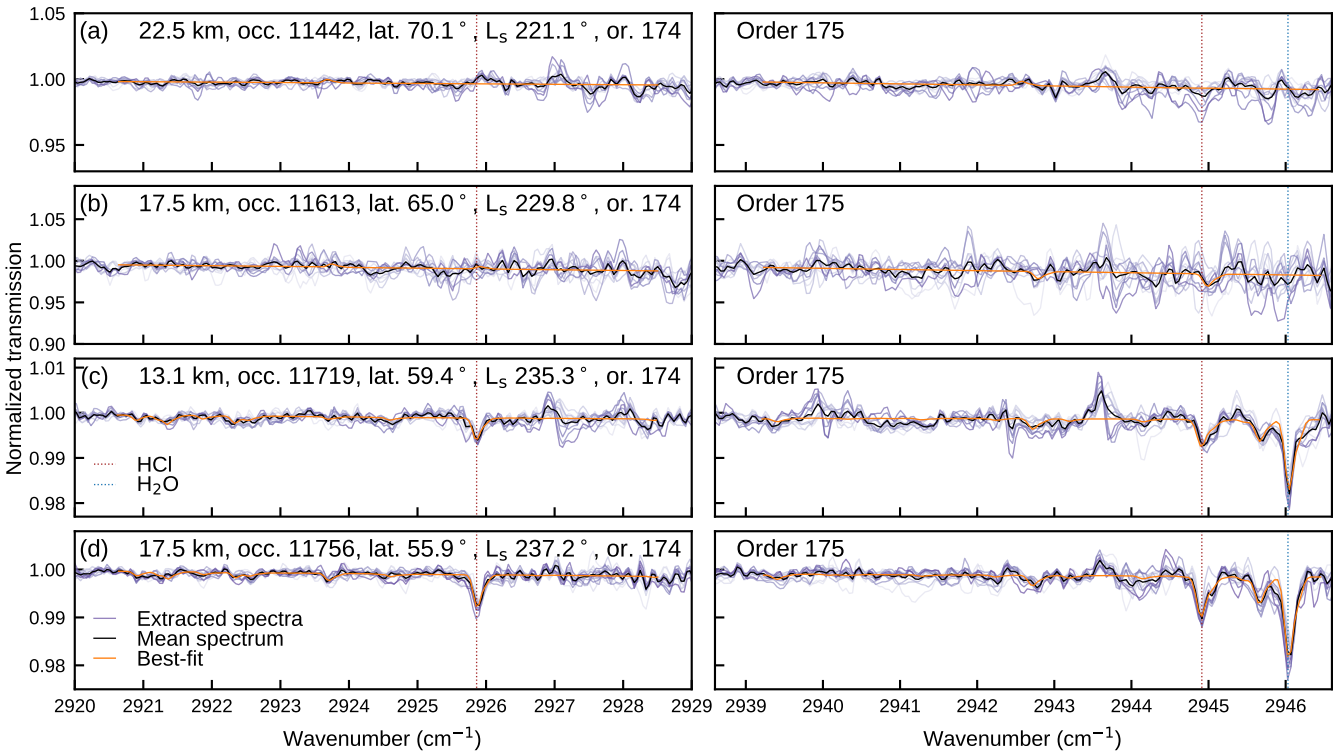

Fig. 1. Measured spectra from diffraction orders 174 and 175 for four occultations recorded between L_s 220 and 240 at high northern latitudes. Shown are the individual spectra extracted from a dozen detector rows covering the same diffraction orders (shades of purple). Also shown are the mean spectra with reduced noise, and best-fit lines for the mean spectra. Positions of major HCl and H_2O lines are indicated with dashed vertical lines in orange and blue, respectively. The first two occultations, panels a and b, do not feature a detectable quantity of HCl or water vapour, while the later occultations, panels c and d, feature 0.5 and 0.9 ppbv HCl and around 60 and 120 ppmv H_2O, respectively.

echelle grating, providing access to diffraction orders with infrared spectral ranges, followed by a secondary diffraction grating that separates the diffraction orders. Details about the instrument and data processing, including images of the raw detector frames, can be found in Korablev et al. (2018); Trokhimovskiy et al. (2020); Olsen et al. (2021). The secondary grating can be rotated into different positions to adjust the spectral orders available, and therefore the instantaneous spectral range covered in a measurement. HCl lines are present in two configurations of the ACS MIR detector, with the secondary grating rotated to positions 11 and 12.

At each tangent altitude observed, a vertical field of view of several kilometres is recorded by a two dimensional detector, resulting in 20 rows of unique spectra for each diffraction order separated by 175 m. Past analyses have used only single rows extracted from the detector frame due to differences in temperature, pressure aerosol loading, and instrument line shape between rows. Here, we exploit the full field of view to improve the sensitivity and accuracy of our retrievals. 12 detector rows are extracted, and each set of solar occultation spectra is analyzed separately to obtain vertical profiles of HCl VMR. We then take the weighted mean and the standard error of the weighted mean to represent the most accurate estimate of the true VMR.

The design of the instrument intended to use the set of spectra for each order to further reduce the spectral noise, enhancing the sensitivity of ACS MIR to trace gas detections. However, two factors have previously led us to not pursue this. First, there is an issue with one of the optical elements that can impact the instrument line shape by giving the appearance that an absorption line has a double image (for a detailed description of this issue see Alday et al. (2019); Olsen et al. (2021)). The magnitude of the double image changes among the rows recorded for a diffraction order, so computing a mean can effectively reduce the spectral resolution. Second, each unique spectrum from an order is at a different tangent altitude and the aerosol loading in the Martian atmosphere is enough to create differences in the baseline levels between each spectrum. In order to compute a mean spectrum, each unique spectrum must first be normalized, which may increase the noise when the transmittance is low. Furthermore, each row contributing to the mean is recorded at different tangent altitudes with different pressures and temperatures, so those parameters needed to analyze the mean spectrum are less certain.

In position 11, the strongest HCl lines that are free from interference from CO_2 and HDO lines are found in diffraction orders that lie on the very bottom of the two-dimensional detector frame. In this area there is almost no impact of the doubling. Therefore, for this study we have exploited the size of the detector array to obtain more accurate HCl retrievals. First, we will demonstrate the ability of ACS MIR instrument to definitively detect a rare trace gas by computing mean spectra, then we will mitigate errors caused by the tangent altitude differences by performing vertical profile VMR retrievals on each detector row and finding the mean VMR profile, rather than performing a profile retrieval on the mean spectra. The latter method is computationally intensive, but gives a clear idea of the true uncertainty of the retrievals made using single spectra while very effectively increasing the retrieval accuracy and reducing the uncertainty.

Fig. 1 shows mean spectra recorded in the northern hemisphere at around 20 km from four different solar occultations made between L_s = 220–240°. The first two occultations, panels a and b, show no detectable quantities of HCl. The remaining

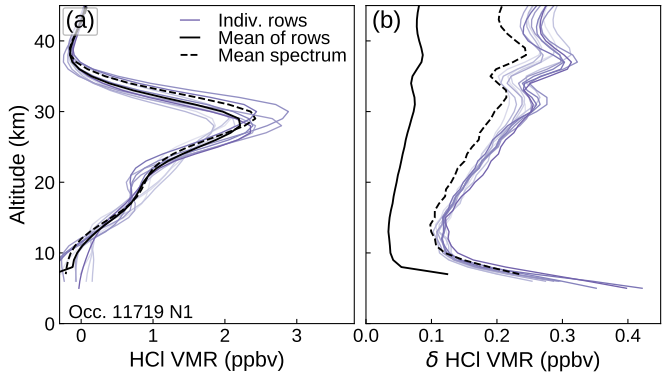

Fig. 2. Example retrieved vertical profile of HCl during the Mars year 35 dust season. *Panel a*: an ensemble of retrieved vertical profiles (shades of purple, as in Fig. 1) made for one occultation. Each line corresponds to a set of detector rows from which spectra were extracted. *Panel b*: the corresponding ensemble of uncertainties. In panels a and b, the solid black lines show the weighted mean of the ensemble of retrievals, and the uncertainty (standard error). The dashed black lines are for a retrieval made using the mean spectra shown in Fig. 1.

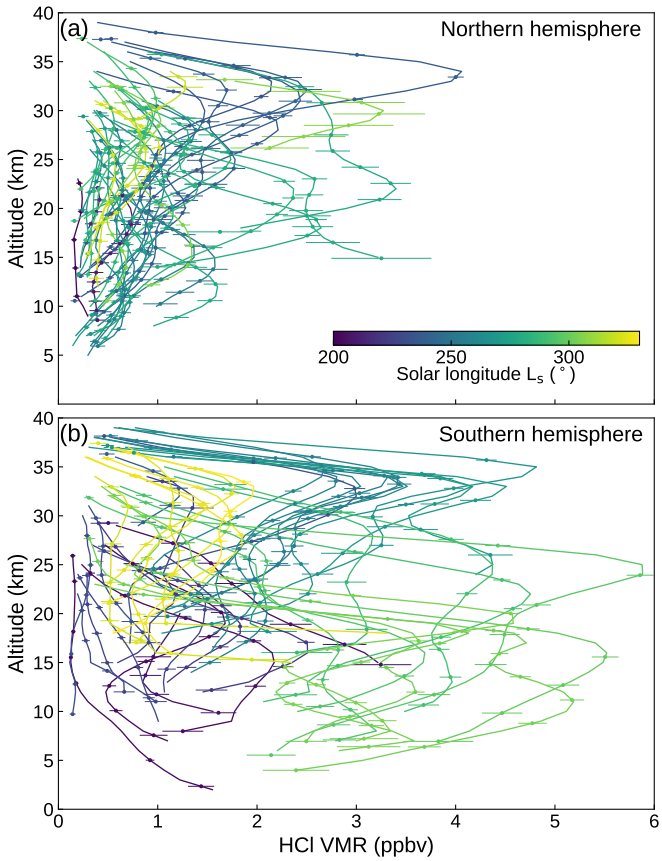

Fig. 3. Retrieved vertical profiles of HCl during the Mars year 35 dust season. The mean retrieved HCl VMR vertical profiles for each occultation made in *a*: the northern hemisphere, and *b*: the southern hemisphere during Mars year 35. Colours indicate solar longitude, L_s.

two occultations, panels c and d, clearly show the appearance of absorption lines caused by HCl and water vapour. Each panel in Fig. 1 shows portions of two diffraction orders that contain HCl absorption features: 174 (2910–2935 cm^{-1}) and 175 (2925–2950 cm^{-1}). For each diffraction order, at each tangent altitude, 12 spectra are extracted from the detector frame around the row in which the solar signal is maximum, which has the the optimal signal-to-noise ratio. In Fig. 1, these are shown in shades of purple, and a mean spectrum is shown in black. We can see that the spectral noise is generally random, and that the noise level of the mean lines is strongly reduced relative to the envelope created by the individual lines. Some systematic features, for example near 2943.6 cm^{-1}, are remnants of the transmission calibration and are at the position of strong solar lines.

We consider an HCl detection to be unambiguous when a 5-σ statistically significant VMR retrieval is made and the HCl line depths extend beyond the noise level in several diffraction orders and at more than three tangent altitudes. The mean spectra shown in Fig. 1 allow us to unambiguously determine whether HCl is present, even when the quantity is small enough that absorption line depths are not much greater than the noise found in individual spectra (e.g., Fig. 1c). On the other hand, however, this also allows us to reject the potential of false-positive identification that may have occurred in, e.g., order 175 in Fig. 1b.

While it is possible to use the mean spectra for VMR vertical profile retrievals, a more accurate approach is to create an ensemble of retrievals for the twelve rows considered. This allows the differences in tangent altitude, ILS, temperature, and pressure to be accounted for. This is a very powerful approach and can reduce the VMR uncertainty dramatically (Fig. 1b).

Spectral fitting and VMR vertical profile retrievals have been done using the JPL Gas Fitting software suite (GFIT or GGG) (Sen et al. 1996; Irion et al. 2002; Wunch et al. 2011). Vertical profiles of temperature and pressure at the terminator are first either retrieved independently using coincident measurements made with the ACS near-infrared channel (NIR) Fedorova et al. (2020), or estimated with the LMD general circulation model (LMD GCM) (Forget et al. 1999; Millour et al. 2018; Madeleine et al. 2011) using the climatology for the atmospheric dust loading for MY 34 and MY 35 (Montabone et al. 2020). Line parameters are taken from the HITRAN 2016 line list and use H_2O broadening parameters for a CO_2-rich atmosphere (Gordon et al. 2017; Gamache et al. 2016; Olsen et al. 2019). Spectral fitting is performed over a set of spectral windows between 2796–2947 cm^{-1} (orders 167-175, depending on availability) containing available HCl and H_2O lines that are the strongest and most-free of interference. A matrix of mean number densities along the optical path is inverted with a matrix of slant paths to estimate the VMR vertical profiles and their uncertainties (Olsen et al. 2021, 2020; Korablev et al. 2020).

Fig. 2a and b shows an example of the retrievals for a single occultation, panel a shows the ensemble of retrievals made using the 12 sets of spectra extracted from each row of the detector frame. The envelope that these profiles create gives an indication of the uncertainty that should be assigned to a retrieval using a single set of spectra. The dominant causes of the differences are from spectral noise, errors in fitting the ILS, and errors in determining the tangent altitude and assigning pressures and temperatures. Fig. 2b shows the VMR uncertainties for the ensemble of retrievals showing a dramatic increase towards the lowest altitudes where the signal has become attenuated by dust, and a gradual increase towards higher altitudes as the number density falls off.

Fig. 2a also shows the weighted mean profile in black and the profile retrieved from the mean spectra as a dashed line. Fig. 2b shows that using the the mean spectra (dashed black), with reduced spectral noise, results in smaller VMR uncertainties. It also shows that the standard error of the weighted mean (black) is smaller again by more than a third (approximately $1/\sqrt{12}$).

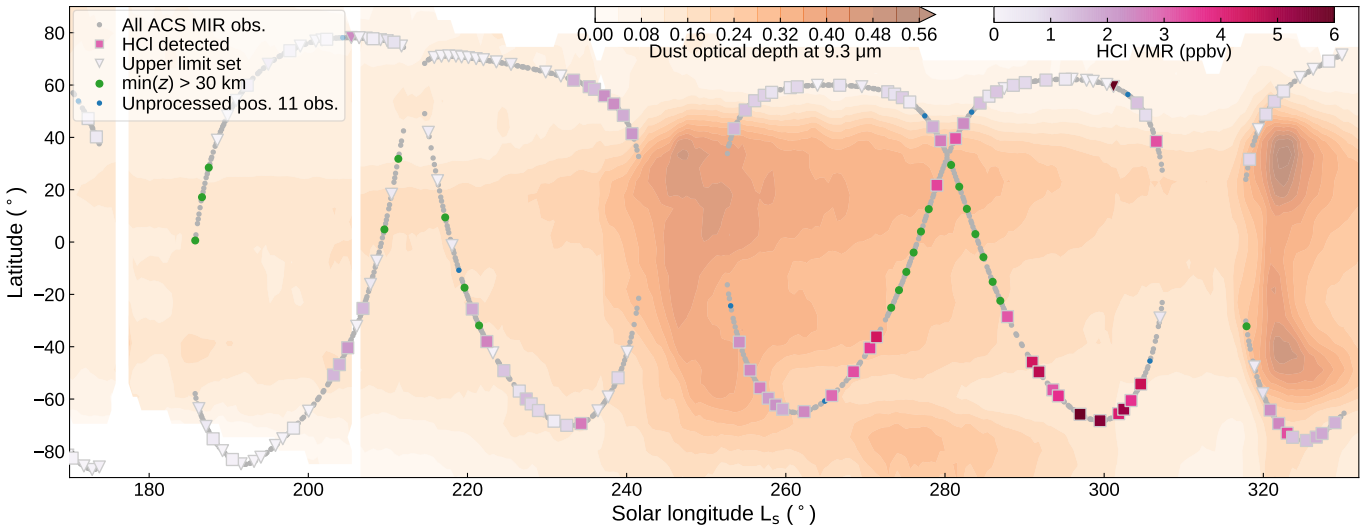

Fig. 4. The distribution of dust and ACS MIR occultation tangent points during the Mars year 35 dust season. The background, in orange, shows the derived climatology of dust for MY 35 as observed by the Mars Climate Sounder Montabone et al. (2020) (zonal means at each time step). Over this is plotted the latitude of ACS MIR occultations made in MY 35 as a function of solar longitude (L_s) for the period L_s = 160–300°. All ACS MIR occultations are grey, those made using position 11 in which HCl was detected are squares coloured according to the maximum HCl VMR observed below 30 km. Observations where only an upper limit of HCl could be made are shown as triangles, those where the atmosphere below 30 km is obscured by aerosols are indicated in green, and occultation not yet processed are blue.

We note that the shape of the retrieved profiles above 30 km is impacted by the gradual disappearance of HCl lines within the noise level of ACS MIR spectra as number density falls off rapidly with altitude. The HCl VMR does not necessarily tend to zero as rapidly as shown. However, retrieved abundances below that are consistent within the ensemble of rows (Fig. 2a), and statistically significant (Fig. 3, discussed below).

The immediate impact of using the mean retrievals for the ensemble of detector rows is a removal of ambiguity in the retrievals caused by random error, and a sharp reduction of the uncertainties. There are two practical results of this. The first is that the usable altitude range is extended. The usable altitude range is defined as those tangent altitudes in which a retrieved VMR is significant at a 5 σ level. For the example used in Fig. 2a, the usable altitude range is 13–32 km observed at eight tangent levels. The second, is that this method results in statistically significant retrievals of HCl VMRs between 0.1–0.4 ppbv, which is on the order of the detection limits established previously (Korablev et al. 2020). This has implications for establishing a background level of HCl outside the perihelion dust season.

3. HCl and dust in MY 35

The mean VMR profiles, and their uncertainties, retrieved after the start of the MY 35 dust season are shown in Fig. 3, grouped by latitude into northern and southern hemispheres. While we see the near simultaneous appearance of several ppbv of HCl in both hemispheres again, as in MY 34, there is a strong difference in the time evolution between hemispheres. In the southern hemisphere, where HCl is first observed, Fig. 3b, we initially see 0.3–2 ppbv below 20 km, with the first observations revealing HCl only below 10 km. After L_s = 253°, we see HCl at higher altitudes, with 2–3 ppbv between 20–30 km, and a VMR that is increasing over time. From L_s = 280 – 310° we observe the highest quantities of HCl, 4-6 ppbv, but now at lower altitude, and after L_s = 310°, we begin to see a decline in HCl abundances. The vertical change in the altitudes at which HCl is observed is consistent with the observed impact that aerosols have on ACS MIR transmittances over the same time period (which may also limit how low ACS MIR observations can be made). The evolution of aerosol loading is shown in Fig. A1. In the northern hemisphere, Fig. 3a, we observe a very sudden increase in HCl VMRs, with peak HCl activity occurring between L_s = 233–256°, and we observe HCl VMRs decreasing after. There are several observations between L_s = 270 – 300° in which we see 2-3 ppbv around 20 km, and these are at lower latitudes than the majority of profiles shown in Fig. 3a (see Fig. 4). These observation are also consistent with observed changes in dust loading (see Fig. A1).

The time evolution of HCl observations during the MY 35 perihelion period is presented in Fig. 4, which shows the latitudes of ACS solar occultations over L_s. Fig. 4 also shows the climatology of the column dust optical depth at 9.3 μm for MY 35. The methodology used to produce daily maps of column dust optical depth from Mars Climate Sounder observations is the same as for MY 34, described in Montabone et al. (2020). These observations reveal an increase in the dust opacity after L_s = 180°, when seasonal changes begin to warm the southern hemisphere, ushering in the perihelion dust season. Dust activity picks up between L_s = 220–230°, after which a large dust storm was observed. A second, brief period of intense dust activity occurs after L_s = 320°, similar to that seen in MY 34. The spatial distribution of dust activity before, during, and after its peak are shown in Fig. A2.

The observational track in the northern hemisphere in Fig. 4 begins with an equatorial crossing near L_s = 180°, followed by several mid-latitude observations in which the impact of aerosols have already begun to obscure the lower atmosphere for solar occultation measurements (refer also to Fig. A1). This is followed by a period of high northern latitudes observations in which no significant quantity of HCl is observed. After L_s = 232°, as the latitudes observed fall below 60°N, we observe a rapid increase in HCl up to 4 ppbv. After the peak of the dust storm season, and a gap in ACS MIR observations, we continue to consistently observe HCl at high northern latitudes, but at lower VMRs, about 1 ppbv.

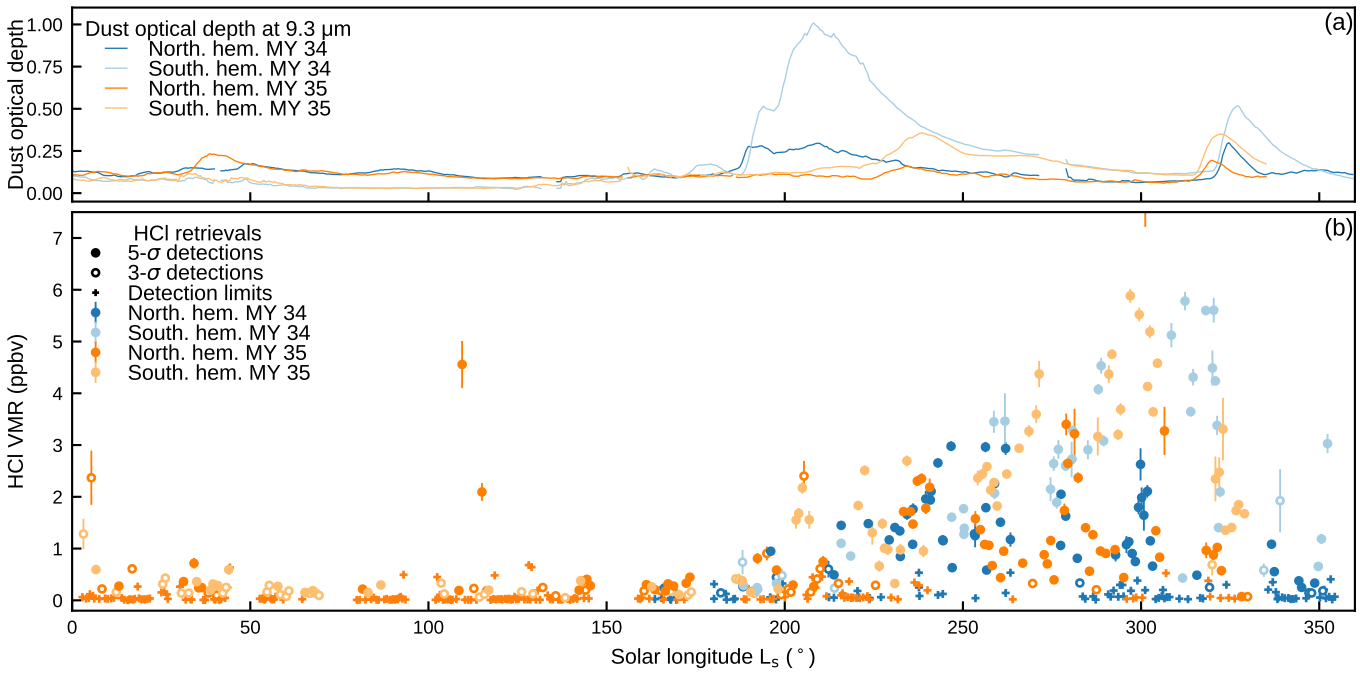

Fig. 5. Time evolution of HCl detections and the meridional column dust opacities for Mars years 34 (blue) and 35 (orange). Panel a shows the dust optical depth at 9.3 μm derived from Mars Climate Sounder Montabone et al. (2020). The mean column dust opacities are first zonally averaged, then a meridional average is shown. The meridional averages are taken over bands covering the northern hemisphere (40–70°N) and southern hemisphere (40–70°S). Panel b shows the maxima of ACS MIR HCl detections below 30 km (circles). For observations in which no HCl was detected at a 5-σ level, a 3-*sigma* criteria is first used (open circles), and if not met detection limits are given (crosses).

In the southern hemisphere, we have a period before L_s = 203° or near-polar observations with very low, or no HCl abundances. The first unambiguous detection of HCl is made at mid-southern latitudes on L_s = 203°, followed by several subsequent detections. As the observational track crosses the equator, we either do not observe HCl, or aerosol loading prevents observations of the lower atmosphere. After L_s = 220°, we begin to observe significant quantities of HCl again and consistently see ~ 1 ppbv throughout the far southern latitudes. After peak dust activity, we observe 2–4 ppbv between L_s = 250–270°, followed by a series of observations obscured by aerosols. The time evolution of the aerosol attenuation in these observations is shown in Fig. A1.

There are two observational constraints in the ACS MIR observations that limit our interpretation of these data. The first is a drawback of the solar occultation geometry that results in the latitudinal arcs seen in Fig. 4, favouring observations towards the poles, rarely sampling activity towards the equator, the region of peak dust activity. Secondly, the main effect of dust loading on solar occultation observations is to limit the lower altitude levels at which we can record transmission spectra. Since HCl is restricted to the lower atmosphere, below 30–35 km, it is impossible to observe during peak dust activity because ACS MIR often cannot see below 30 km. This is the case, for example, with the southern hemisphere observations between L_s = 235–245°, and was discussed in Korablev et al. (2020). It is possible that ACS MIR observations of HCl are made outside of the airmasses where HCl is produced, revealing changes in the atmosphere following intense dust activity, rather than during it.

Though the MY 35 dust season is far less active than that in MY 34, which produced the global dust storm, the column dust optical depths from both season are compared in Fig. 5. Shown for each year are zonal and meridional averages for latitude bands covering the ACS observations (40–70°N and 40–70°S). Fig. 5 shows the HCl VMR maxima and upper limits for the entire ACS MIR data set from L_s = 163° in MY 34 through L_s = 280° in MY 35. Dust loading after L_s = 230° is similar in both years. The MY 34 observations presented in Korablev et al. (2020) have been reprocessed here using the full vertical field of observations (only position 11 occultations are shown, and vertical profiles are reproduced in Fig. A4). In both MY 34 and MY 35, HCl was observed nearly simultaneously with the onset of dust activity in the perihelion season, with the largest VMRs observed shortly after storms (note that we could not observe the lower atmosphere during the MY34 dust storm). Outside this time period, HCl is either not observed, or is generally a tentative detection of < 0.4 ppbv, with the exception of two occultations described in detail below. In both Mars years we also note higher VMR values in the southern hemisphere (lighter colours) relative to the north, similar to hemispheric differences in dust loading.

While we observe a temporal correlation between HCl appearance and dust activity at perihelion, we do not observe a correlation between the HCl abundances shown in Fig. 4 or 5 and the column dust opacity at the tangent locations of our observations. This is partially due to the differences in viewing geometry, which means we are comparing observations sensitive to different altitudes, but may also result from the relative rates of HCl production and dust sedimentation wherein gaseous HCl is produced in the early phase of the storm, builds up and then remains while dust is receding. The thermal infrared channel of ACS (TIRVIM) has been used to measure vertical profiles of the dust mass loading Luginin et al. (2020). Only ten ACS solar occultation measurements have been made in which both TIRVIM dust retrievals and HCl detections were made (shown in Fig. A3). A correlation between the magnitude of dust mass loading and HCl abundance is not observed over altitude, but these do confirm that HCl is observed at altitudes containing dust (0.2-1.0 $\times$ 10^{-11} g cm^{-3} at 10–30 km), but above the layers with

highest dust mass ($1–3\times10^{-11}$ g cm^{-3} below 10 or 20 km, which is the lower limit of these ACS MIR observations due to the dust attenuation).

4. Discussion

The ACS MIR observations presented here and in Korablev et al. (2020) demonstrate a seasonality of HCl activity that is synchronous with the perihelion dust activity. Crucially, we observe similar behaviour, though with different abundances and time evolution, towards both poles, in contrast with the seasonal changes in temperature and water vapour. Such periodic activity is not likely to be produced only by surface outgassing events, although these are still a possibility. The remaining source of HCl is photochemical, while atmospheric dynamics may also help explain our observations.

There is a possibility that there is a persistent quantity of HCl in the lowest layers of Martian atmosphere and that the dynamical effects of dust storms elevate the surface HCl in the same manner as water vapour. A limitation of the solar occultation technique is that ACS MIR is often not able to observe the atmosphere in the first few kilometres closest to the surface. However, previous searches for HCl considered the total column abundance and still set upper limits on 0.2–0.6 ppbv Hartogh et al. (2010); Villanueva et al. (2013). Furthermore, HCl is expected to a have lifetime on the order of years in the Martian atmosphere, and should be well-mixed, assuming only photolysis and neglecting heterogeneous chemistry on the aerosols. Thus a plausible explanation of our results could include dust-driven atmospheric dynamics, possibly combined with dispersed surface emission. We continue to treat this as only a partial solution for two reasons: a strong dynamical effect has been observed during GDS events, but we observe a similar quantity of HCl in MY 35 as in MY 34, when the dust activity was less severe, limiting its impact on atmospheric heating, and its ability to drive increasing Hadley cell circulation; HCl is not generally observed during northern summer, a season similarly characterized by warmer temperatures and increased water vapour content in the lower atmosphere (> 100 ppmv below 20 km) (e.g., Montmessin et al. 2017; Fedorova et al. 2020).

It is noteworthy that there are periods where we observe water vapour while not observing HCl, while we are able to show that there is a correlation between HCl and water vapour during the dusty perihelion period when HCl is observed. Water would play a prominent role in photochemical HCl production, but requires a potential chloride source, such as from dust (Korablev et al. 2020). The data initially reported in Korablev et al. (2020) did not support a quantitative correlation between the H_2O and HCl mixing ratios over altitude, but the new data from MY 35 and the reprocessed data from MY 34 do. This is due to an increase in the sample size of data available (the new analysis technique increases the vertical range of usable HCl retrievals) and in their accuracy. The changes in time of the shape of the HCl profiles track the evolution of water vapour in both Mars years, and the Pearson correlation coefficient for the entire data set is 0.73. The ensembles of simultaneous H_2O vertical profiles corresponding to the data in Fig. 3 are shown in Fig. A5 along with correlation scatter plots (MY 34 is shown in Fig. A4). Water vapour is still observed at altitudes higher than HCl (and also above the top of the aerosol layer), and in occultations when HCl is not detected, for example, during most of the northern summer. HCl lines are not found in ACS MIR spectra without the presence of water vapour lines.

Additionally, with the new techniques presented here, small quantities of HCl, between 0.1–0.4 ppmv were frequently found at a 3–5-σ level during the aphelion time period in both hemispheres, as shown in Fig. 5. At this level, HCl absorption features are on the order of the spectral noise, and these quantities could not previously be detected using single spectra. Even with the mean profiles, these detections are at the very limit of the capabilities of ACS MIR, with HCl features embedded within the noise envelope of the ensemble of spectra at each altitude.

Of special interest are the two data points near L_s = 110° in Fig. 5 where we see uncharacteristically elevated levels of HCl outside the perihelion dust season. These were made at mid-northern latitude in the Arcadia region, north of Alba Mons (66°N,117°W) and (46°N,97°W)). In these occultations, we are able to probe down to below 5 km above the surface (common during this time period). HCl lines are distinct up to above 10 km, and these are considered unambiguous. They differ considerably from the profiles shown in Fig. 3 in that HCl is constrained to below 10 km and the mixing ratios shown in Fig. 5 are found at the lowest altitudes. Water vapour is observed in both cases, also in the lower atmosphere. Ensembles and means of their VMR vertical profiles and spectra are shown in the Fig. A6 and A7.

One of these observations is among the ten in which we have coincident profiles of dust mass loading from (Luginin et al. 2020). Here again, dust is observed at the same altitudes at which we observe HCl. Other northern hemisphere TIRVIM observations from the same time period L_s = 107.5–107.5° reveal consistency among the dust mass loading profiles, but other ACS MIR observations used for HCl detection reveal no HCl at the same altitudes (note that these are not coincident measurements). A map of the column dust opacity and locations of ACS observations is shown in the Fig. A8, with the coincident vertical profiles of dust and HCl VMR. These very limited aphelion dust observations are not inconsistent with the observations made at perihelion due to the northern summer dust and water activity.

When reporting our initial discovery, we noted that the rapid disappearance of HCl after the GDS was difficult to explain by photochemical or dynamical means. However, the solution may be a combination of a portion of the HCl remaining in the lower atmosphere, downward transport migrating HCl from 20–30 km to < 5 km, and photochemical destruction or deposition.

Thus, we propose that the observations made by ACS MIR support a coupling between the surface and atmospheric reservoirs of chlorine. The mechanism for such a coupling remains unidentified, but is based on known chemistry in the terrestrial atmosphere, and is likely to be combined with the strong dynamical effects related to dust activity.

On Earth, sodium chloride (NaCl) in sea salt is transported into the atmosphere where it becomes hydrated and may react with acids (e.g., HNO_3 or H_2SO_4). The hydrated aerosols may immediately liberate chloride ions, or reactions on the aerosol surfaces may directly lead to HCl formation of the release of volatilized chloride radicals (e.g., George & Abbatt 2010; Simpson et al. 2015). On Mars, chloride is widespread (Osterloo et al. 2008, 2010; Murchie et al. 2009; Wray et al. 2009; Glotch et al. 2010; Ruesch et al. 2012) and resides primarily in the form of NaCl (Glotch et al. 2016). The availability of such acids (HNO_3 and H_2SO_4) on Mars remains unverified, so a more direct pathway is proposed wherein the hydration of NaCl is sufficient to release Cl^- ions. Available chloride radicals will readily oxidize, mainly via HO_2, to produce HCl (Catling et al. 2010). Laboratory studies have shown that such a pathway is viable (Sjostedt & Abbatt 2008), and also that Martian conditions are sufficient

to hydrate aerosols (Santiago-Materese et al. 2018), which was the case during the MY 34 GDS (Fedorova et al. 2020). Furthermore, nitrates have been identified on the surface of Mars and should make up a component of lofted dust (Stern et al. 2017); in addition, the presence of nitrates should lead to acid formation (Smith et al. 2014).

The first direct measurement of the mineral composition of chloride-bearing soil components was made by the Phoenix lander, which discovered perchlorates (ClO_4^-) (Hecht et al. 2009). The possible origin of surface perchlorates was unexplained and motivated several laboratory and modelling studies to resolve its origin. This effort accelerated after Curiosity also identified perchlorate (Glavin et al. 2013) and its distribution was posited to be widespread on Mars (Clark & Kounaves 2016). Much of the experimental work done concerning chlorides on Mars supports the formation of perchlorates directly on the surface over long periods (e.g., Rao et al. 2012a; Carrier & Kounaves 2015; Zhao et al. 2018; Civiš et al. 2019), often demonstrating direct pathways to convert NaCl to ClO_4^-. Catling et al. (2010) proposed an atmospheric source of surface perchlorate that is the end-product of ancient atmospheric HCl of volcanic origin. This was shown to be insufficient to produce the observed abundances of perchlorate (Smith et al. 2014), and Wilson et al. (2016) showed that radiolysis on the surface can release chloride from salts, which may then sublimate into the atmosphere where it will eventually form perchlorate and be deposited out of the atmosphere. Further studies have also shown that more exotic mechanisms, invoking electric discharges and plasma chemistry, may also release Cl from chloride salts Rao et al. (2012b); Wu et al. (2018); Martínez-Pabello et al. (2019); Wang et al. (2020).

A common theme among these studies is that perchlorate is a sink for chlorine. Gas-phase HCl is either not considered, or it has no photochemical source, often assuming a volcanic HCl source (Catling et al. 2010; Smith et al. 2014; Wilson et al. 2016). None of the proposed mechanisms for perchlorate formation, nor the resulting Martian surface chlorine chemistry, suitably explain the observations of HCl made by ACS MIR in MY 34 and 35. Our observations imply that HCl is formed in the lower part of the atmosphere, below 40 km, shortly after the start of dust activity, whether it is extreme, as in MY 34, or regular, seasonal activity, as in MY 35. After the dust subsides, so does the HCl. A component of the removal of HCl will also be downward transport as the atmosphere cools (Heavens et al. 2018; Neary et al. 2020; Fedorova et al. 2020), and there may also be unconstrained photochemical pathways and deposition related to the dust itself (e.g., Sullivan et al. 2007), and uptake on water ice aerosols (Kippenberger et al. 2019; Korablev et al. 2020). Altogether, the rapid removal of HCl as observed by ACS MIR is at odds with the current photochemical theory which predicts that HCl is the long-lived, permanent reservoir of chlorine.

5. Conclusions

The ACS MIR instrument on the ExoMars Trace Gas Orbiter has been used to observe solar occultation transmission spectra in a region containing HCl absorption lines over a period from $L_s = 163°$ in Mars year 34 to $L_s = 282°$ in MY 35 (2.5 Earth years). During this time, two perihelion dust seasons were observed, with a global dust storm occurring in MY 34. During both dusty periods, HCl is observed at high latitudes in both hemispheres below 40 km with mixing ratios of 1–4 ppbv. We note a moderate-to-strong correlation between HCl and water vapour (0.73), which would be needed for photochemical production pathways of HCl. We observed rapid temporal evolution of the HCl mixing ratios that was distinct in each hemisphere. HCl is generally not observed during the aphelion period, when dust loading is low, even during northern summer, when water vapour is present. However, on two occasions, close together in time and location, we observed HCl at levels greater than 2 ppbv below 10 km during the aphelion period.

The distribution over latitude and time of perihelion HCl detections is unlikely to be caused by periodic outgassing events, but such activity is not ruled out. Following our initial discovery of HCl after the MY 34 GDS, we proposed a possible photochemical pathway related to NaCl-bearing dust aerosols that is analogous to tropospheric chemistry on Earth. The second appearance of HCl in MY 35 following increased dust activity supports this possibility, but does not prove it. Further laboratory experiments are needed to show that HCl can be formed from airborne, hydrated NaCl aerosol, and at what rate. Circulation modelling studies are needed to show what role transport plays in explaining our observations, and photochemical modelling studies are needed to explain the removal, over the course of tens of sols, of HCl following its detection, in contradiction with the long HCl lifetime predicted by the conventional photochemistry.

Acknowledgements. The ACS investigation was developed by the Space Research Institute (IKI) in Moscow, and the Laboratoire Atmosphères, Milieux, Observations Spatiales (LATMOS/CNRS) in Paris. The investigation was funded by Roscosmos, the National Centre for Space Studies of France (CNES) and the Ministry of Science and Education of Russia. The GGG software suite is maintained at JPL (tccon-wiki.caltech.edu). This work was funded by the Natural Sciences and Engineering Research Council of Canada (NSERC) (PDF–516895–2018), the UK Space Agency (ST/T002069/1) and the National Centre for Space Studies of France (CNES). All spectral fitting was performed by KSO using the GGG software suite. The interpretation of the results was done by KSO, AT, FL, FM and OK. The processing of ACS spectra is done at IKI by AT and at LATMOS by LB. Input and aid on spectral fitting were given by JA, DB, CFW, PGJI, AF, and FM. The ACS instrument was designed, developed, and operated by AP, AS, AT, FM, and OK. Climatologies of dust optical depth for MY 34 and MY 35 were provided by LM and vertical profiles of dust mass were produced by ML. Vertical profiles of measured temperature and pressure were generated by AF, and terminator temperatures and pressures where modelled by FF, EM, and AB.

References

Alday, J., Wilson, C. F., Irwin, P. G. J., et al. 2019, Astron. Astrophys., 630, A91
Aoki, S., Vandaele, A. C., Daerden, F., et al. 2019, J. Geophys. Res., 124, 3482
Carrier, B. L. & Kounaves, S. P. 2015, Geophys. Res. Lett., 42, 3739
Catling, D. C., Claire, M. W., Zahnle, K. J., et al. 2010, J. Geophys. Res., 115, E00E11
Civiš, S., Knížek, A., Rimmer, P. B., et al. 2019, ACS Earth Space Chem., 3, 221
Clark, B. C. & Kounaves, S. P. 2016, Int. J. Astrobiol., 15, 311
Fedorova, A. A., Montmessin, F., Korablev, O., et al. 2020, Science, 367, 297
Forget, F., Hourdin, F., Fournier, R., et al. 1999, J. Geophys. Res., 104, 24155
Gamache, R. R., Farese, M., & Renaud, C. L. 2016, J. Mol. Spectrosc., 326, 144
George, I. J. & Abbatt, J. P. D. 2010, Nat. Chem., 2, 713
Giardini, D., Lognonné, P., Banerdt, W., et al. 2020, Nat. Geosci., 13, 1
Glavin, D. P., Freissinet, C., Miller, K. E., et al. 2013, J. Geophys. Res., 118, 1955
Glotch, T. D., Bandfield, J. L., Tornabene, L. L., Jensen, H. B., & Seelos, F. P. 2010, Geophys. Res. Lett., 37, L16202
Glotch, T. D., Bandfield, J. L., Wolff, M. J., Arnold, J. A., & Che, C. 2016, J. Geophys. Res., 121, 454
Gordon, I. E., Rothman, L. S., Hill, C., et al. 2017, J. Quant. Spectrosc. Radiat. Transfer, 203, 3
Hartogh, P., Jarchow, C., Lellouch, E., et al. 2010, Astron. Astrophys., 521, L49
Heavens, N. G., Kleinböhl, A., Chaffin, M. S., et al. 2018, Nat. Astron., 2, 126
Hecht, M. H., Kounaves, S. P., Quinn, R. C., et al. 2009, Science, 325, 64
Irion, F. W., Gunson, M. R., Toon, G. C., et al. 2002, Appl. Opt., 41, 6968
Kass, D. M., Schofield, J. T., Kleinböhl, A., et al. 2019, Geophys. Res. Lett., 46
Kippenberger, M., Schuster, G., Lelieveld, J., & Crowley, J. N. 2019, Atmos. Chem. Phys., 19, 11939
Korablev, O., Montmessin, F., Trokhimovskiy, A., et al. 2018, Space Sci. Rev., 214, 7

Korablev, O., Olsen, K. S., Trokhimovskiy, A. andLefèvre, F., et al. 2020, Sci. Adv., in press
Luginin, M., Fedorova, A. A., Ignatiev, N. I., et al. 2020, J. Geophys. Res., 125, e2020JE006419
Madeleine, J. B., Forget, F., Millour, E., Montabone, L., & Wolff, M. J. 2011, J. Geophys. Res., 116, E11010
Martínez-Pabello, P. U., Navarro-González, R., Walls, X., et al. 2019, Life Sci. Space Res., 22, 125
Millour, E., Forget, F., Spiga, A., et al. 2018, in From Mars Express to ExoMars, 68
Montabone, L., Spiga, A., Kass, D. M., et al. 2020, J. Geophys. Res., 125, e06111
Montmessin, F., Smith, M. D., Langevin, Y., Mellon, M. T., & Fedorova, A. A. 2017, in The Atmosphere and Climate of Mars, ed. R. M. Haberle, R. T. Clancy, F. Forget, M. D. Smith, & R. W. Zurek, Cambridge Planetary Science (Cambridge University Press), 338–373
Murchie, S. L., Mustard, J. F., Ehlmann, B. L., et al. 2009, J. Geophys. Res., 114, E00D06
Neary, L., Daerden, F., Aoki, S., et al. 2020, Geophys. Res. Lett., 47, e84354
Olsen, K. S., Boone, C. D., Toon, G. C., et al. 2019, J. Quant. Spectrosc. Radiat. Transfer, 236, 106590
Olsen, K. S., Lefèvre, F., Montmessin, F., et al. 2021, Nat. Geosci.
Olsen, K. S., Lefèvre, F., Montmessin, F., et al. 2020, Astron. Astrophys., 639, A141
Osterloo, M. M., Anderson, F. S., Hamilton, V. E., & Hynek, B. M. 2010, J. Geophys. Res., 115, E10012
Osterloo, M. M., Hamilton, V. E., Bandfield, J. L., et al. 2008, Science, 319, 1651
Rao, B., Estrada, N., McGee, S., et al. 2012a, Environ. Sci. Technol., 46, 11635
Rao, B., Mohan, S., Neuber, A., & Jackson, W. A. 2012b, Water Air Soil Pollut., 223, 275
Ruesch, O., Poulet, F., Vincendon, M., et al. 2012, J. Geophys. Res., 117, E00J13
Santiago-Materese, D. L., Iraci, L. T., Clapham, M. E., & Chuang, P. Y. 2018, Icarus, 303, 280
Sen, B., Toon, G. C., Blavier, J.-F., Fleming, E. L., & Jackman, C. H. 1996, J. Geophys. Res., 101, 9045
Simpson, W. R., Brown, S. S., Saiz-Lopez, A., Thornton, J. A., & von Glasow, R. 2015, Chem. Rev., 115, 4035
Sjostedt, S. J. & Abbatt, J. P. D. 2008, Environ. Res. Lett., 3, 045007
Smith, M. D. 2019, J. Geophys. Res., 124, 2929
Smith, M. L., Claire, M. W., Catling, D. C., & Zahnle, K. J. 2014, Icarus, 231, 51
Stern, J. C., Sutter, B., Jackson, W. A., et al. 2017, Geophys. Res. Lett., 44, 2643
Sullivan, R. C., Guazzotti, S. A., Sodeman, D. A., et al. 2007, Atmos. Environ., 41, 7166
Trokhimovskiy, A., Perevalov, V., Korablev, O., et al. 2020, Astron. Astrophys., 639, A142
Villanueva, G. L., Mumma, M. J., Novak, R. E., et al. 2013, Icarus, 223, 11
Wang, A., Yan, Y., Jolliff, B. L., et al. 2020, J. Geophys. Res., 125, e06283
Wilson, E. H., Atreya, S. K., Kaiser, R. I., & Mahaffy, P. R. 2016, J. Geophys. Res., 121, 1472
Wray, J. J., Murchie, S. L., Squyres, S. W., Seelos, F. P., & Tornabene, L. L. 2009, Geology, 37, 1043
Wu, Z., Wang, A., Farrell, W. M., et al. 2018, Earth Planet. Sci. Lett., 504, 94
Wunch, D., Toon, G. C., Blavier, J. L., et al. 2011, Phil. Trans. R. Soc. A, 369, 2087
Zhao, Y.-Y. S., McLennan, S. M., Jackson, W. A., & Karunatillake, S. 2018, Earth Planet. Sci. Lett., 497, 102

Appendix A: Supplementary Figures

This Appendix contains figures supplementary to the main discussion.

Fig. A1 shows the mean level of non-normalized spectra from diffraction order 174, which is a measure of the amount of attenuation the solar signal is subject to as it passes through the limb of the atmosphere. This is generally caused by aerosols, and may be a combination of dust and ices. The lines are coloured by the measured dust optical depth at 9.3 μm derived from Mars Climate Sounder Montabone et al. (2020) observations over the ACS MIR tangent locations. The upper panels show northern hemisphere observations, while the lower panels show southern hemisphere observations. They are divided into time periods that follow the discussion of Fig.4. Panel a shows the equatorial crossing of the latitude track after L_s = 180° where low- and mid-latitude observations are affected by a high-altitude aerosol layer. Panel b shows a series of near-polar latitudes where the atmosphere is very transparent. This is followed by panel c showing the northern latitudes after L_s = 232°. We begin to see aerosol loading above 30 km, which coincide to large dust optical depth values. These are the observations where 1–4 ppbv HCl was observed. Panel d shows the following northern hemisphere period after L_s = 250°, during which we observed moderate HCl VMRs. Panel e shows the period L_s = 280–310° which is similar to panel d in both aerosol loading and HCl abundances.

Panel f covers the southern hemisphere before L_s = 203° in which we do not observe significant dust loading or HCl. Panel g shows latitudinal track between L_s = 203–225° that crosses the equator northward. Here, we see significant aerosol activity at mid and low-latitudes again, and occasionally observed ~ 1 ppbv HCl at lower altitudes. Panel h shows significant dust activity in deep southern latitudes between L_s = 225–245°, during which period we consistently observed 1–2 ppbv HCl. Panel i shows the southern hemisphere observations after L_s = 250° which are characterized by a series of observation with moderate dust at low altitudes, in which we observed 2–4 ppbv HCl, followed by observations made towards the equator in which the aerosol attenuation is observed at higher altitudes, obscuring the lower atmosphere. Finally, panel j shows the penultimate southward latitude ark in Fig.4 between L_s = 280–310° during which we observe highest HCl values, but at lower altitudes. In this panel we see the altitudes where aerosols are present falling.

Fig. A2 shows the spatial distribution of dust at three times during the aphelion period. For each panel, the average dist opacity over 5° L_s is shown, and the locations of ACS observations during that 5° period are plotted. HCl detections and upper limits made using secondary grating position 11 and shown in Fig.4 are indicated. Panel a covers the period L_s = 203–208° when we make the first observations of HCl at mid-latitudes in the southern hemisphere. Panel b covers L_s = 231–236° and shows both peak dust activity and where we make the first observations of HCl in the northern hemisphere. Panel c shows subsided dust activity over L_s = 293–298°, during which we begin have northern observations in which only detection limits are made again. Panel d shows the period between L_s = 321–326°, during which dust activity picked up again briefly.

Fig. A3 shows vertical profiles of dust mass loading derived from simultaneous observations made with ACS TIRVIM Luginin et al. (2020). Panel a shows dust mass loading from three occultations over the northern hemisphere and panel b shows HCl VMRs from coincident ACS MIR observations. Panel c and d show the same data for six occultation in the southern hemisphere. The correlation between dust mass loading and HCl VMR over altitude is low, but this does confirm that dust aerosols are present over the altitude ranges at which we observe HCl.

Fig. A4 and Fig. A5 compares the retrieved vertical profiles of HCl from ACS MIR observations with those of water vapour made from simultaneous ACS NIR observations. Fig. A4 shows results from MY 34 and included the data presented in Korablev et al. (2020) reprocessed with the new technique presented in this work. Fig. A5 contains the data in Fig. 3 up to L_s = 300°. The ACS NIR instrument uses a spectral range with a greater number of H_2O lines, which are also stronger, allowing sensitivity to water vapour at higher altitudes then we are able to observe HCl. ACS NIR observations from MY 34 and during the GDS are published in Fedorova et al. (2020), while those from MY 35 have been produced in a similar manner. Each figure separates northern and southern hemisphere observations, and shows the vertical profiles of HCl, H_2O, and scatter plots directly comparing the two. The scatter plots compare the retrieved VMRs at each tangent height where both gases were observed (ACS NIR measurements are interpolated to heights of ACS MIR measurements). In MY 34, we compute Pearson correlation coefficient of 0.68 and 0.73 in the northern and southern hemispheres, and in MY 35, we find coefficients of 0.83 to the north and 0.68 to the south. Combining all the data results in a correlation coefficient of 0.73 using 679 data points.

Fig. A6 and Fig. A7 show the ensemble and mean retrievals of HCl (upper left) and H_2O (lower left) VMRs for two occultations made in the northern hemisphere during summer (aphelion). These reveal > 2 ppbv HCl below 10 km. The right panels in both figures show the ensemble of spectra used for diffraction orders 173–175, as well as mean spectra, for the three lowest tangent altitudes observed, similar to Fig. 1. HCl lines, at positions indicated with brown dashed lines, are consistently observed above the noise level in all three orders and at several altitudes.

Fig. A8 a shows a map of Mars overlaid with the dust optical depth at 9.3 μm derived from Mars Climate Sounder Montabone et al. (2020), and averaged between L_s = 107.5–117.5°. Shown also are the locations of ACS solar occultation measurements. Those using position 11 are highlighted in blue, and those in which HCl was observed during the aphelion period (Fig. A6 and A7) are highlighted in purple. Norther hemisphere observation in which retrieved vertical profiles of dust mass loading made with coincident TIRVIM observations are available are indicated with black circles. Panel b shows the vertical profiles of HCl VMR and dust mass loading for the coincident measurements at (46°N, 97°W) made on L_s = 115° in MY 35. Other dust mass loading profiles from the north-eastern quadrant are consistent in magnitude and shape. This shows that, though rare, HCl observations made in northern summer may also be related to seasonal dust activity.

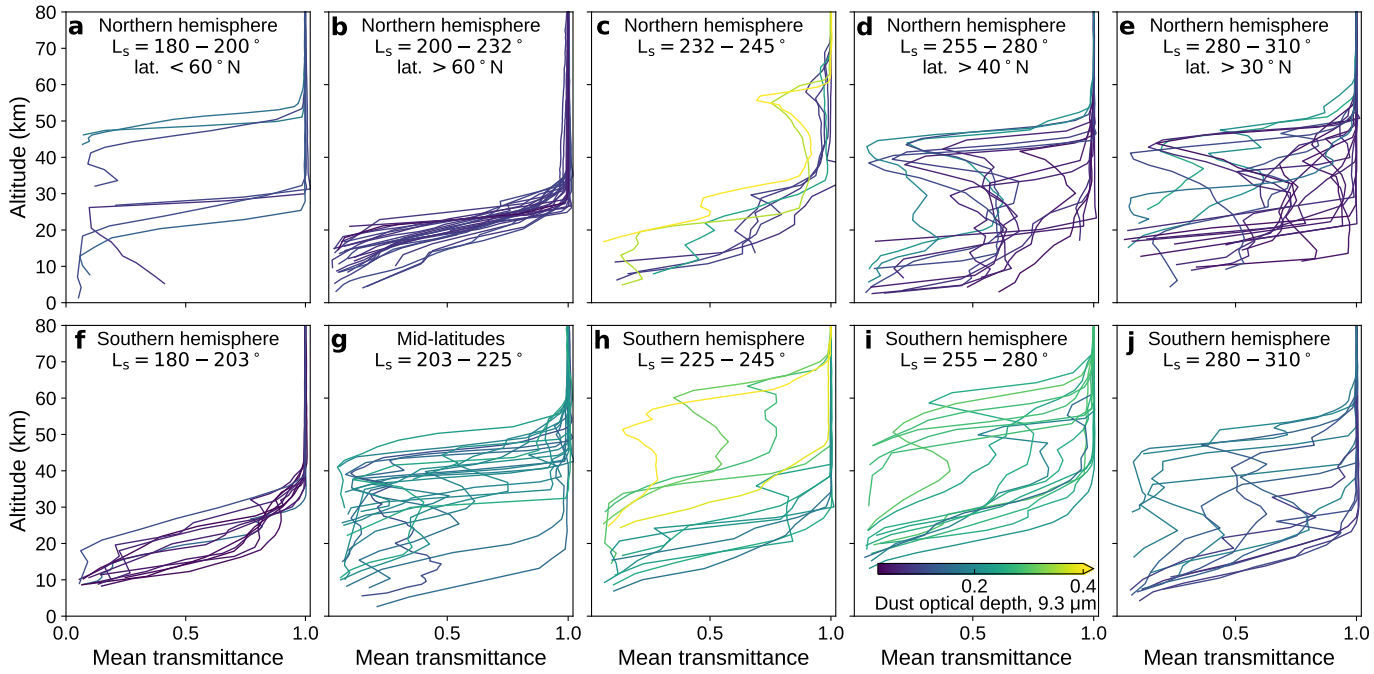

Fig. A1. Time evolution of vertical profiles of the transmission level of solar occultation absorption spectra recorded with ACS MIR. Panels a–d show four time periods in the northern hemisphere that coincide with observed changes in dust activity and the detection of HCl. Panels e–h show the same thing for the southern hemisphere. Lines are coloured by the dust optical depth at 9.3 μm derived from Mars Climate Sounder observations Montabone et al. (2020).

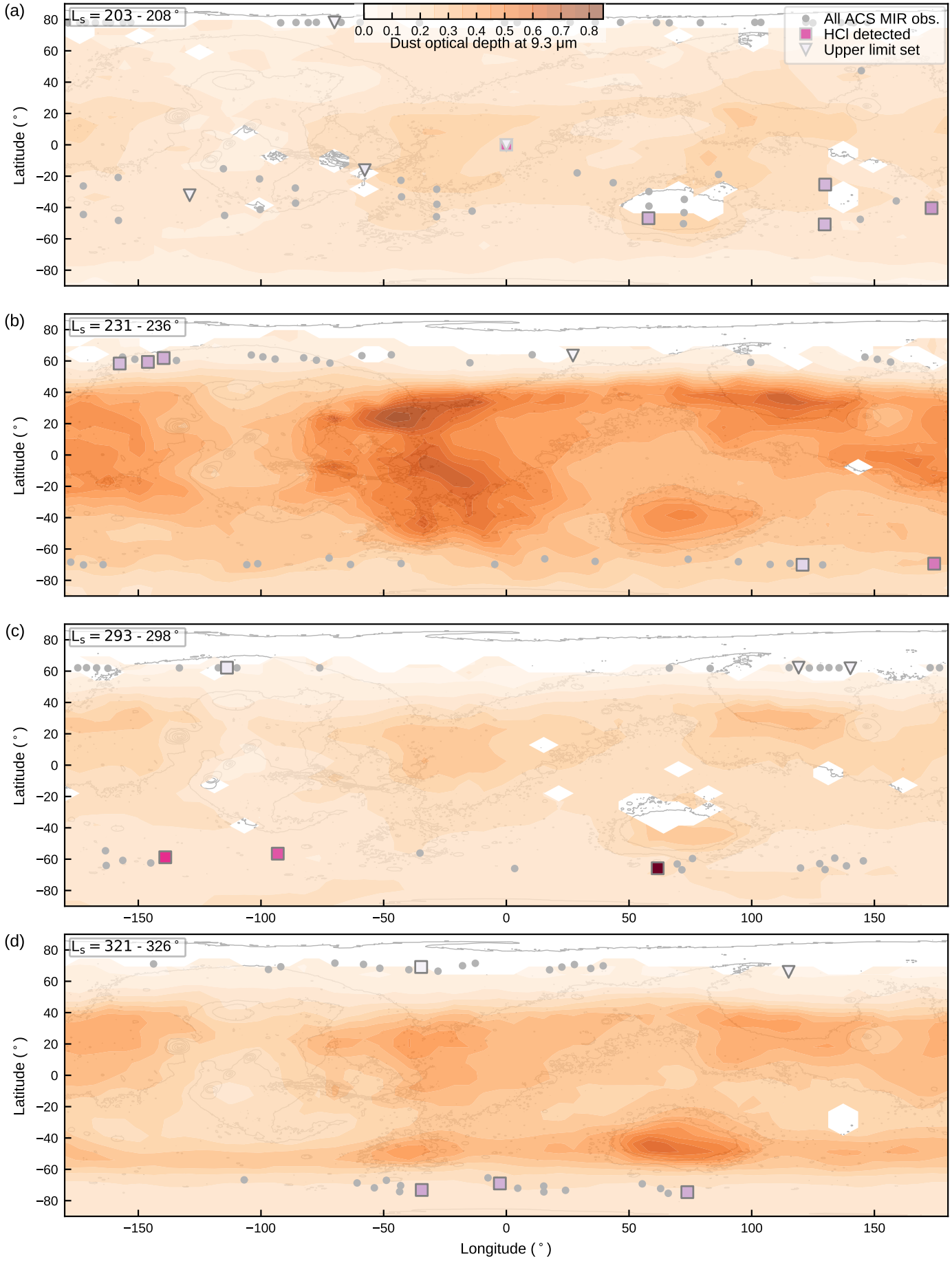

Fig. A2. Spatial distribution of dust optical depth at 9.3 μm derived from Mars Climate Sounder observations Montabone et al. (2020). Three time periods are shown, a: L_s = 203–208°, b: L_s = 231–236° c: L_s = 293–298°, d: L_s = 321–326°.

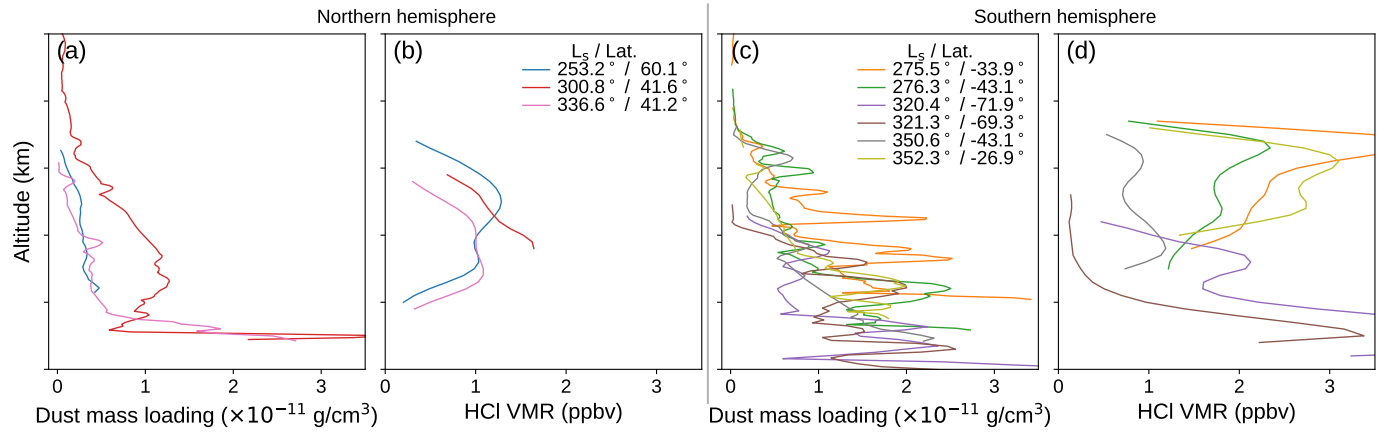

Fig. A3. Coincident measurements of the vertical profiles of HCl VMR and dust mass loading. Panels a and c show dust mass loading retrieved from observations made with ACS TIRVIM from the northern and southern hemispheres, respectively. Panels b and d show retrieved HCl VMR vertical profiles from simultaneous observations.

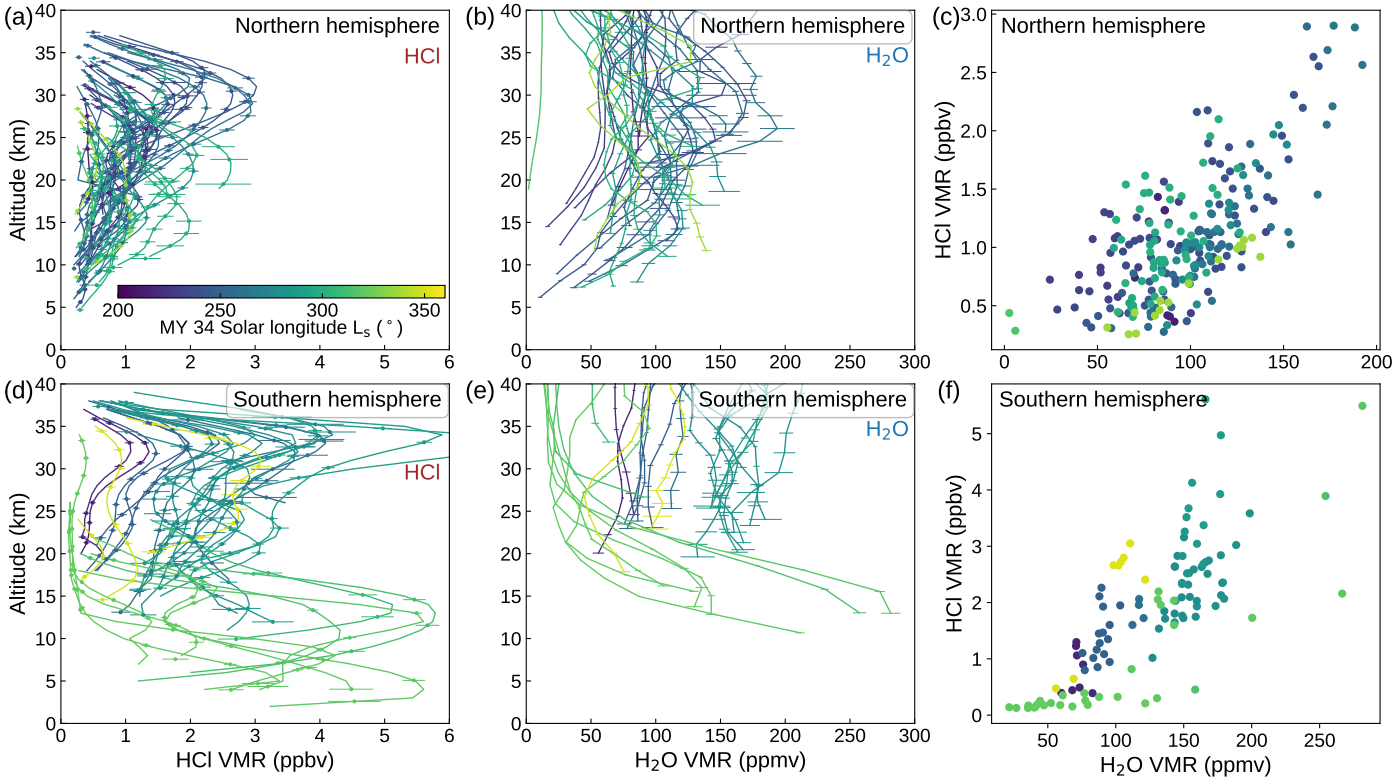

Fig. A4. Comparison of the retrieved vertical profiles of HCl from ACS MIR and H_2O from ACS NIR during MY 34 perihelion. *Panel a*: VMR vertical profiles of HCl from the northern hemisphere. *Panel b*: VMR vertical profiles of H_2O from the northern hemisphere. *Panel c*: Scatter plot comparing northern hemisphere HCl and H_2O at overlapping tangent heights. Pearson correlation coefficient is 0.68. *Panel d*: VMR vertical profiles of HCl from the southern hemisphere. *Panel e*: VMR vertical profiles of H_2O from the southern hemisphere. *Panel f*: Scatter plot comparing southern hemisphere HCl and H_2O at overlapping tangent heights. Pearson correlation coefficient is 0.73.

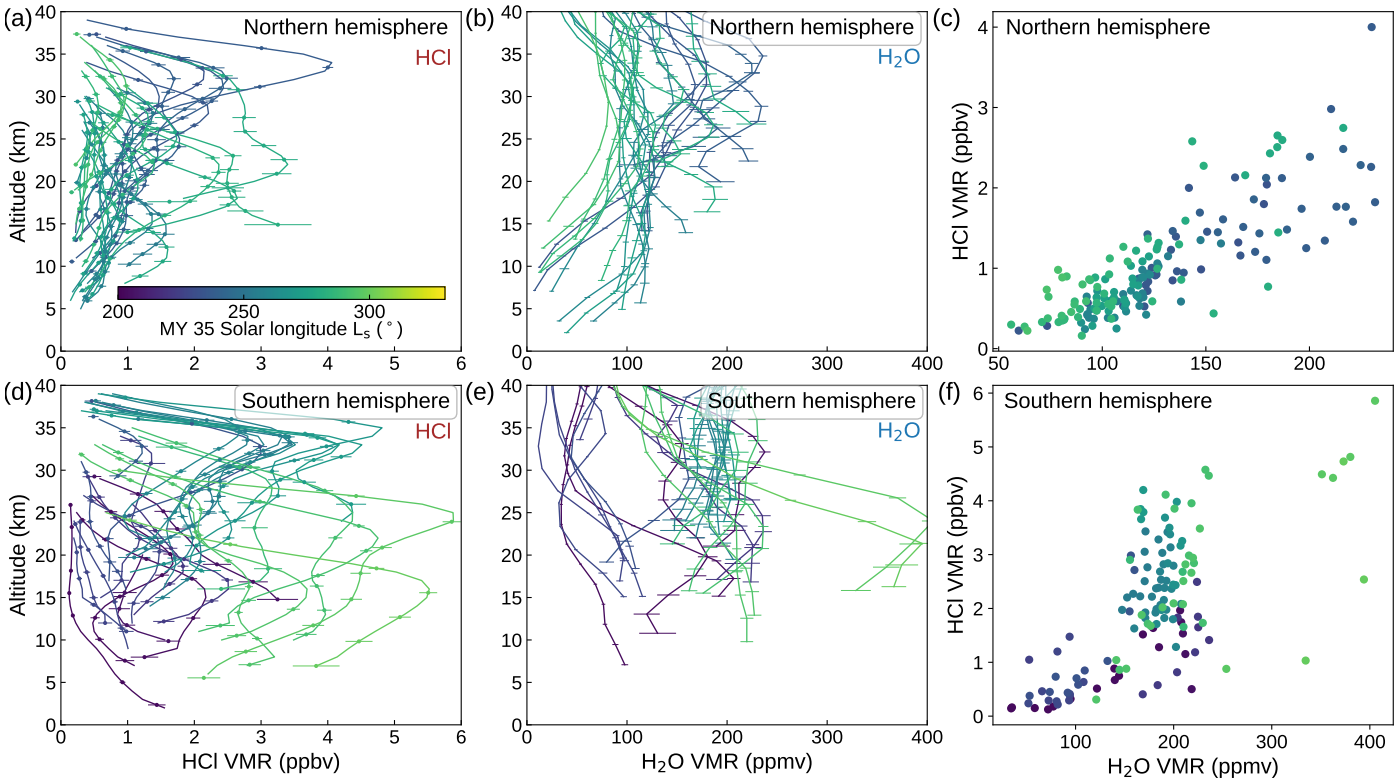

Fig. A5. Comparison of the retrieved vertical profiles of HCl from ACS MIR and H_2O from ACS NIR during MY 35 perihelion. Panels are as in Fig. A4. The Pearson correlation coefficient for panels c (northern hemisphere) and d (southern hemisphere) are 0.83 and 0.68, respectively.

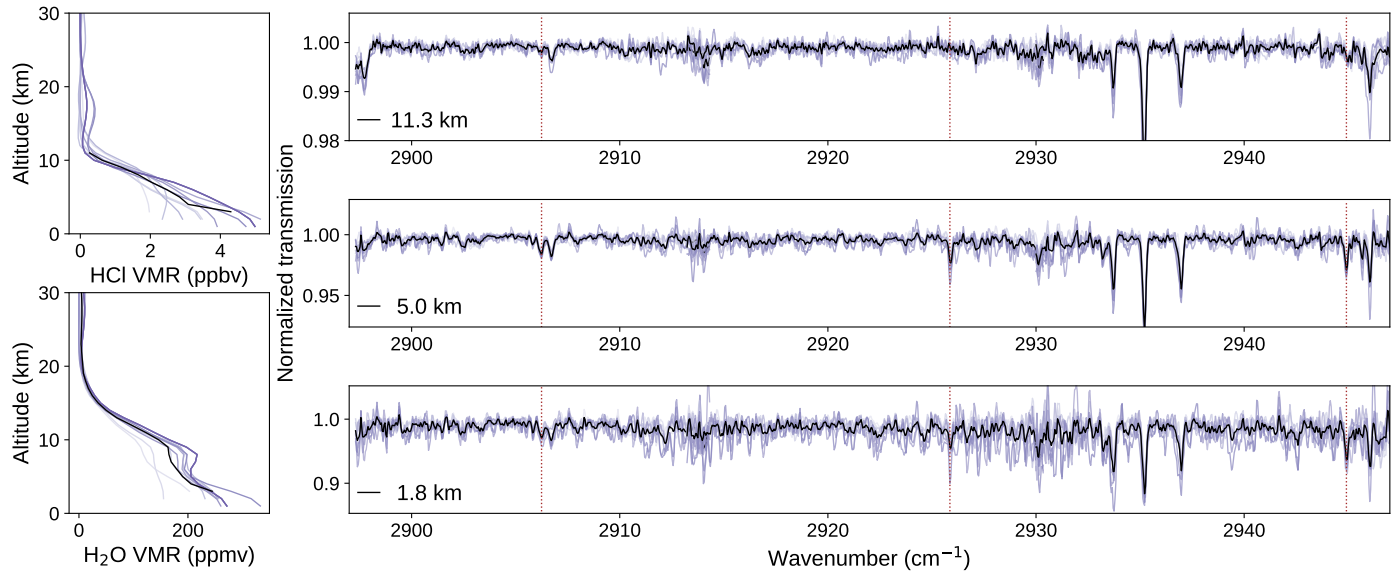

Fig. A6. A look at the HCl (upper left) and H_2O (lower left) VMR vertical profiles, as in Fig. 2, for an occultation made during the aphelion season (L_s = 109.5°) at (66°N, 117°W). The spectra used in the retrieval (orders 173–175) over three tangent heights are shown to the right, as in Fig. 1. HCl and H_2O are constrained to below 15 km. These observations made outside the perihelion dust season are considered robust and may be indicative of local dust events or possible outgassing.

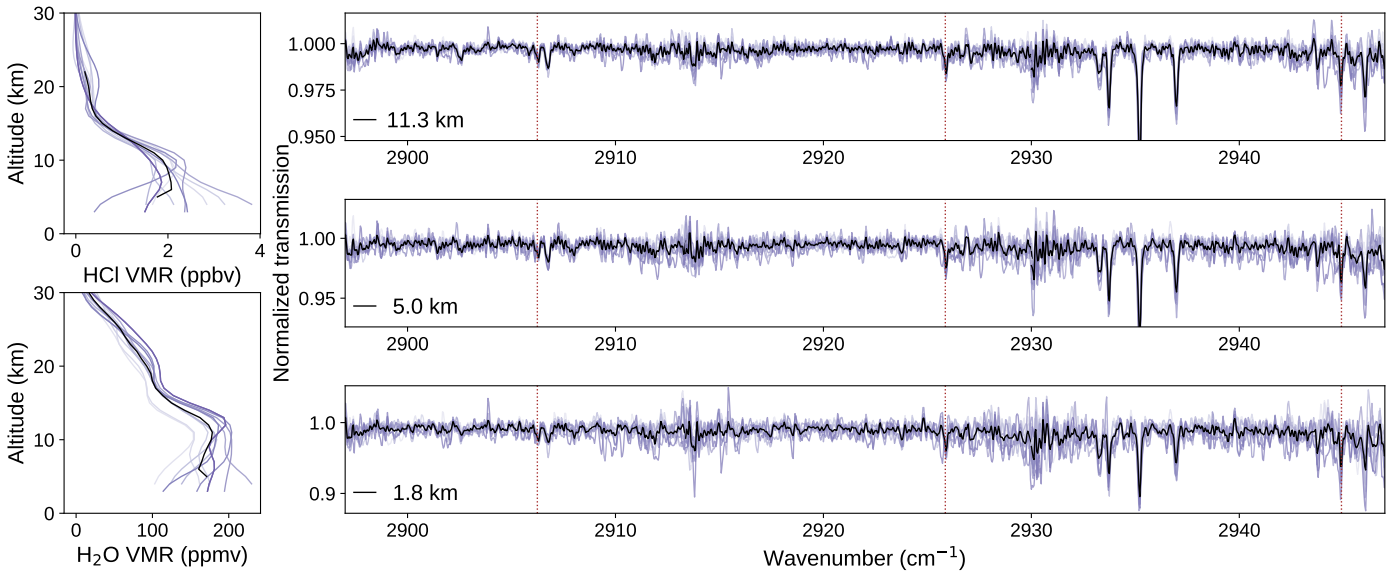

Fig. A7. A look at the HCl (upper left) and H_2O (lower left) VMR vertical profiles, as in Fig. 2, for an occultation made during the aphelion season (L_s = 115°) at (46°N, 97°W). The spectra used in the retrieval (orders 173–175) over three tangent heights are shown to the right, as in Fig. 1. HCl and H_2O are constrained to below 15 km. These observations made outside the perihelion dust season are considered robust and may be indicative of local dust events or possible outgassing.

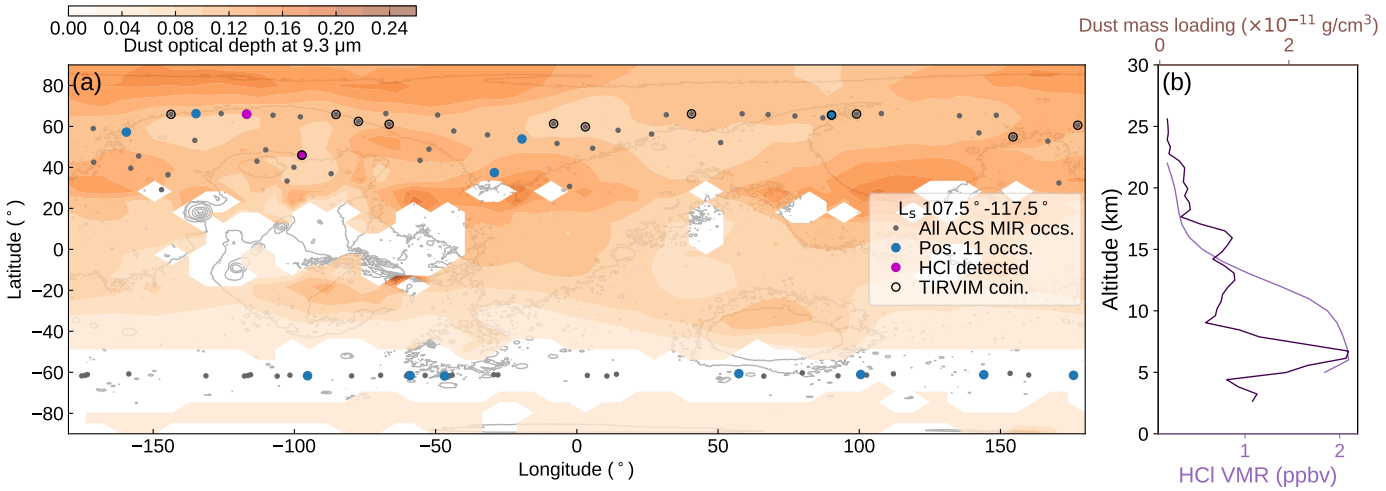

Fig. A8. Panel a shows the spatial distribution of dust optical depth at 9.3 μm Montabone et al. (2020) averaged between L_s = 107.5–117.5° over a map of Mars. Also shown are the tangent point locations of ACS MIR solar occultations. Highlighted are occultations made using position 11, those in which HCl was observed, and those with coincident TIRVIM observation (northern only). Panel b shows the vertical profiles of HCl VMR from ACS MIR and dust mass loading from ACS TIRVIM Luginin et al. (2020) for the coincident observation at (46°N, 97°W).